Particle-in-cell/Monte Carlo collisions treatment of an Ar/O$_2$ magnetron discharge used for the reactive sputter deposition of TiO$_X$ films

E Bultinck[1] and A Bogaerts

Research group PLASMANT, Department of Chemistry, University of Antwerp, Universiteitsplein 1, 2610 Antwerp, Belgium
E-mail: evi.bultinck@ua.ac.be

Abstract. The physical processes in an Ar/O$_2$ magnetron discharge used for the reactive sputter deposition of TiO$_x$ thin films were simulated with a 2d3v particle-in-cell/Monte Carlo collisions (PIC/MCC) model. The plasma species taken into account are electrons, Ar$^+$ ions, fast Ar$_f$ atoms, metastable Ar$_m^*$ atoms, Ti$^+$ ions, Ti atoms, O$^+$ ions, O$_2^+$ ions, O$^-$ ions and O atoms. This model accounts for plasma–target interactions, such as secondary electron emission and target sputtering, and the effects of target poisoning. Furthermore, the deposition process is described by an analytical surface model. The influence of the O$_2$/Ar gas ratio on the plasma potential and on the species densities and fluxes is investigated. Among others, it is shown that a higher O$_2$ pressure causes the region of positive plasma potential and the O$^-$ density to be more spread, and the latter to decrease. On the other hand, the deposition rates of Ti and O are not much affected by the O$_2$/Ar proportion. Indeed, the predicted stoichiometry of the deposited TiO$_x$ film approaches $x = 2$ for nearly all the investigated O$_2$/Ar proportions.

[1] Author to whom any correspondence should be addressed.

IOP Institute of Physics   Φ DEUTSCHE PHYSIKALISCHE GESELLSCHAFT

Contents

1. Introduction

Magnetron discharges have widespread applications in the field of 'sputter deposition' of thin metallic or compound films. In this process, particles with a sufficient amount of energy bombard a target, which initiates a collision cascade in the target, leading to a possible release of a surface atom. This target process is called 'sputtering'. The sputtered atoms pass through the reactor chamber and can be deposited on a substrate, placed in front of the target, forming a thin metallic coating. In our case, the energetic particles originate from argon background gas, which is electrically transformed into a plasma: by coupling an electrical circuit to the target, and putting the other walls at ground potential, the target acts as a cathode and the other walls as anode. Hence, an electric field is generated, which partially breaks down the gas into ions and electrons, i.e. a plasma is created.

    The plasma is magnetically enhanced: by placing magnets behind the cathode target, a magnetic field is created. Charged particles from the plasma circulate around the magnetic field lines with their Larmor radius:

$$r = \frac{mv}{qB}.$$

(1)

The high ion mass causes the ion Larmor radius to be very large, leading to an almost straight movement of the ions. However, electrons have a much lower mass, which causes them to be trapped in the magnetic field. As a consequence, the electrons have longer mean free paths, and therefore a higher probability for ionizing the background gas. When these ions, accelerated by the electric field, hit the cathode target, target material can be sputtered. The enhanced ionization results in a large amount of sputtering, and allows the magnetron discharge to operate at lower pressures (typically in the range of 0.1–1 Pa [1]) in comparison with non-magnetized sputtering discharges. Due to the lower pressure, the sputtered atoms will be less scattered on their way to the substrate. This results in a more effective deposition.

    Most magnetized electrons reside where the radial magnetic field is at a maximum. As a consequence, the ionizations occur in the same area. In the present work, a planar circular magnetron in a cylindrical chamber is investigated, meaning that the magnetron consists of a planar circular cathode on which a planar circular target is clamped. The magnetron is balanced, meaning that the majority of the magnetic flux lines that originate at the cathode, also return to
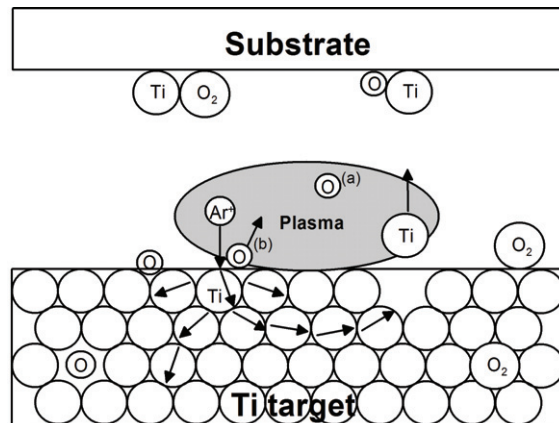
IOP Institute of Physics ⏀ DEUTSCHE PHYSIKALISCHE GESELLSCHAFT

Figure 1. Schematic representation of the reactive sputter deposition process. O atoms, originating from plasma reactions with the O_2 gas (a), or from sputtering the poisoned TiO_x target (b), as well as O_2 gas molecules, can react with sputtered Ti atoms on the substrate to form a TiO_x film.

it without crossing the anode. In a planar balanced magnetron, the maximum plasma density is therefore found in a narrow area in front of the cathode (denoted as a dotted area in figure 1). Therefore, the planar target is locally sputtered, leaving behind an erosion cavity, the so-called 'race-track'.

When a reactive gas, like oxygen, is added to the Ar background gas, the O_2 gas molecules themselves as well as atoms originating from the O_2 gas (by plasma reactions, or by sputtering a poisoned TiO_x target) can react with the sputtered metal atoms on the substrate to form a metal oxide layer [2]–[4], in a process called 'reactive sputter deposition'. This process is schematically presented in figure 1.

However, these reactions between oxide and Ti species can also take place on the sputtering target, causing it to become (partially) oxidized. This target modification process is called 'poisoning'. One major disadvantage of poisoning is that it may drastically reduce the sputtering yield of the target, and consequently the deposition rate [5]. Furthermore, the transition from the so-called 'metallic' to 'reactive' condition happens via a complex and inconvenient hysteresis [6, 7]. However, in order to deposit a stoichiometric TiO_2 film, the reactive gas is necessary. The goal is to find reactive gas/background gas proportions which allow a satisfactory high deposition rate, as well as a stoichiometric deposited film.

Magnetron reactive sputter deposition is studied extensively by experiments (an overview is presented in [8]). These experiments enable to discover and explain relations between external parameters, such as cathode current and voltage, gas pressure and pumping speed, magnetic field, geometrical characteristics of the magnetron, and the measured properties, such as current, voltage, pressure (if they change during the time progression of the discharge), plasma species densities, fluxes and energies, plasma potential distribution, erosion profiles and characterization of the deposited thin film. Some of these characteristics are however more precarious to measure due to possible plasma disturbance with the measuring tool and/or limitations in size of the measuring tool (hence certain areas are not reachable), or cannot be measured at all (for instance information on separate collision processes). However, to validate the developed numerical models, experiments remain inevitable. Moreover, certain input parameters are required in models, which need to be measured experimentally. Therefore, the combination of experiments

and numerical models is desirable to provide a complete chemical and physical picture of magnetron discharges, needed to optimize the applications.

Different kinds of models exist to simulate gas discharges. Mostly, these models are subdivided into analytical, continuum and particle models, as well as hybrid models which comprise combinations of these aforementioned models.

'Analytical models' are based on simple analytical (mostly (semi-)empirical) formulae to describe the behavior of macroscopic plasma characteristics, such as voltage, current, pressure and magnetic field. These models are very fast, but they are limited in accuracy (because approximations are used) and generality (for example, they are only valid for discharge conditions in specific ranges). For magnetron discharges, analytical models exist to predict quickly some general relations between macroscopic plasma characteristics [9]–[15]. The reactive sputter deposition process is modeled in [5, 16, 17], by means of balance equations of the particle fluxes toward these surfaces.

'Continuum or fluid models' are based on the continuity equations and calculate the electric field in a fast and self-consistent way. It is hence a very powerful modeling approach, if the 'local field approximation' is fulfilled, i.e. the charged particles' energies must be in equilibrium with the electric (and magnetic) field. In other words, the energy loss by the collisions must balance the energy gain by the fields, and the plasma must behave as a continuum or a fluid. Fluid models are widely used to simulate gas discharges; however, modeling magnetron discharges with a fluid model is not so common, since they cannot be simply considered as a fluid. Indeed, in a low pressure discharge, such as a magnetron discharge, the loss of energy caused by collisions is much smaller than the energy gain due to the electric field, especially for electrons. Furthermore, the complexity of the magnetic field makes a continuum model for magnetron discharges very inefficient [18]. Nevertheless, in some papers [19, 20] magnetron discharges are simulated by fluid models.

'Hybrid models' denote mostly the combination of Monte Carlo (MC) or particle-in-cell model/Monte Carlo collisions (PIC/MCC) descriptions for the fast electrons, and fluid approaches for all the other species (slow electrons, ions and neutrals). However, the same difficulties arise as for fluid models.

'Particle models' treat every species individually, and hence these models do not have to obey the condition of continuum models. An example is an MC model [21], which treats the collisions probabilistically, and calculates the particles' movements, starting from an initially defined electric field distribution. This modeling technique is rather fast, because the electric field is not calculated self-consistently from the external electrical circuit and the spatial distribution of the charged particles. However, to make the MC model self-consistent, this model can be coupled to a so-called PIC model [22]–[24], which calculates the electric field in a self-consistent manner. The coupled model is named PIC/MCC model [23, 24], and is able to produce a wealth of data, such as cathode voltage and current, plasma species densities, fluxes and energies, potential distribution and information on separate collisions. PIC/MCC models calculate the entire discharge behavior very accurately; however, this goes in expense of a longer calculation time, which is partially accounted for by representing real particles by a limited number of superparticles (SPs), and by weighting the SPs on a grid (hence the name 'PIC'). However, permanently evolving computational devices (fast computers) and methods (code parallelizing) make these methods nowadays very attractive.

Magnetron sputter deposition is investigated by MCC models [25], and more precisely, the reactive sputter deposition was studied in [26]. PIC/MCC models for sputter deposition in

a pure Ar discharge are extensively developed [23, 24], [27]–[32]. To the authors' knowledge, one PIC/MCC model exists for an Ar/O_2 gas mixture [33]. However, this PIC/MCC model does not take into account plasma–surface interactions, such as target sputtering, target poisoning, and atom sticking, i.e. the sputter deposition process itself is not described. Moreover, these plasma–surface interactions influence all of the calculated discharge characteristics [6, 7]. Secondly, the external circuit is not included in the model of [33]. Nevertheless, the external circuit occurs to be inevitable in a PIC/MCC code for an accurate and correct description of magnetron discharges [34].

In our opinion, the PIC/MCC modeling approach produces the most accurate data, making it a very powerful tool to simulate magnetron discharges. However, a complete PIC/MCC model does not yet exist to describe the reactive sputter deposition in an Ar/O_2 gas mixture in a magnetron discharge. Therefore, to study the reactive magnetron sputter deposition process of TiO_x layers, a PIC/MCC model including plasma–surface interactions is developed and presented in this paper.

In the present work, the effect of the O_2/Ar ratio on I–V characteristics, on the plasma potential distribution and on different plasma species densities is calculated. Moreover, sputtered Ti and O fluxes from the target are calculated for different O_2/Ar proportions, as well as Ti, O and O_2 fluxes to the substrate. The coupled analytical surface model enables to describe the deposition process of the TiO_x film, in terms of the deposited TiO_x fraction, the Ti and O deposition rates and the film stoichiometry x.

2. Description of the model

In the PIC/MCC model, the particle movement is simulated with the PIC method, and the collisions are treated with the MCC module. Plasma–surface interactions, such as sputtering, electron emission, species reflection and the effect of a poisoned target, are accounted for in our model. A brief overview, with definitions of certain characteristics and coefficients, is given here. Overviews of the PIC/MCC model can be found in [18], [22]–[24], [32, 34]. A detailed description of a similar model developed for an Ar/N_2 discharge can be found in [35].

The species present in the discharge (electrons, Ar^+ ions, fast Ar_f atoms, metastable Ar_m^* atoms, Ti^+ ions, Ti atoms, O^+ ions, O_2^+ ions, O^- ions and O atoms) are represented by SPs with a corresponding weight factor, describing the amount of real particles per SP. In the PIC algorithm, the properties of the different particles, such as the densities, are calculated on a grid. Weighting the particles' positions to a grid gives the charged particle density on the grid. The potential distribution V is calculated from the densities of the negative species (electrons and negative ions) n_- and the densities of the positive ions n_+:

$$\frac{1}{r}\frac{\partial}{\partial r}r\frac{\partial V}{\partial r} + \frac{\partial}{\partial z}\frac{\partial V}{\partial z} = -\frac{q}{\epsilon_0}(n_+ - n_-).\tag{2}$$

This equation is solved with the superposition principle, presenting the potential V as the sum of the potential only due to the space charge, V_P, and the potential only due to the cathode voltage, U_0, i.e. $V = V_P + U_0 V_L$. U_0 is calculated from the coupling of the external circuit to the plasma, and V_L is the dimensionless potential caused by an applied voltage with magnitude 1 V. A detailed description can be found in [34]. The new electric field distribution E is calculated from V:

$$\mathbf{E} = -\nabla V.\tag{3}$$

After weighting the electric field on the grid back to the particles' positions, the motion of the charged SPs in the electric and magnetic fields are calculated with Newton's equations:

$$m\frac{d\mathbf{v}}{dt} = q\,(\mathbf{E} + \mathbf{v} \times \mathbf{B}),$$

$$\frac{d\mathbf{x}}{dt} = \mathbf{v}. \tag{4}$$

Note that the electric field is both externally applied as well as created by the charged SPs themselves, whereas the magnetic field is only externally applied. The neutrals are not influenced by the present electric and magnetic fields.

The SPs in the discharge can also interact with each other, described in the MCC algorithm. The different plasma reactions can be subdivided into elastic and inelastic collisions. Depending on the type of collision, the total kinetic energy is conserved (elastic collisions) or not (inelastic collisions). In the latter case, the energy is partly consumed as internal chemical energy for one of the collision partners (such as excitation, ionization, dissociation and dissociative ionization), or created and supplied to the discharge as light or heat (such as deexcitation and recombination). The probability of occurrence of the various collisions is dependent on the speed of the incident particle (v), the density of the target species (n_{tar}) and a collision probability, which is based on the collision cross section (σ), or on the reaction rate constant (k). The collision probability for collision j is presented as

$$P_j = 1 - \exp\left(-\Delta t \cdot n_{tar} \cdot v \cdot \sigma_j\,(E_i)\right) \quad \text{or} \quad P_j = 1 - \exp\left(-\Delta t \cdot n_{tar} \cdot \frac{v}{\langle v \rangle} \cdot k_j\,(E_i)\right). \tag{5}$$

Some cross sections of ion–neutral collisions are described with the Langevin–Hasse model [36, 37], assigned 'LH' in table 1, since no other data were available in the literature. This approach calculates the reaction cross section, based on the dimensionless impact parameter for which the deflection angle is negligibly small [38] (assumed 3 for all species [37]), and on the masses, velocities and polarizability of the colliding species (11.08 a_0^3 for Ar [39], 10.60 a_0^3 for O_2 [39] and 5.4 a_0^3 for O [39], where a_0 is the Bohr radius).

After the collision, the SPs are scattered from their original part, and their new velocities (direction and magnitude) are based on the center of mass theory [40], with a characteristic scattering angle, which is dependent on the type of collision. This scattering angle is mostly isotropic in all directions, except for electrons, where the scattering angle depends on the energy of the electron. Further details about their treatment for a magnetron discharge in argon are given in [23, 32]. The collisions included in the model are summarized in table 1. Note that certain species that are present in the discharge are not followed in the model, since they are not very relevant, such as O_3 (which is created by reactions (49) and (50)).

Apart from interactions in the plasma, SPs can also interact with the reactor walls, after which reflection (and/or neutralization), adsorption or the creation of new SPs can occur. The latter can be the creation of secondary electrons, whose yield is characterized by the secondary electron emission coefficient (SEEC), or sputtered atoms, determined by the sputter yield formula of Matsunami *et al* [41]. Reflection of electrons is determined by the reflection coefficient, whereas heavy particles reflection is characterized by the sticking coefficient (SC). If a particle's SC is zero, the particle is reflected when hitting a wall. For Ar atoms, an SC of zero is assumed, since Ar is an inert gas. All included ions are assumed to neutralize after reflection at the walls, which implies that they also have a zero SC, since they are reflected,

Table 1. List of the collisions considered in the model. The references where the cross sections ($\sigma(E)$) or rate constants (k) were adopted from are presented in the last column. The rate constants are in $m^3 s^{-1}$ for two-body collisions and $m^6 s^{-1}$ for three body collisions (indicated by *). '(a)' refers to assumed rate constants based on similar reactions, due to lack of data in the literature. 'LH' refers to the Langevin–Hasse treatment for the cross section (see section 2).

e^- collisions				
(1)	$e^- + Ar \rightarrow e^- + Ar$	Elastic scattering	$\sigma(E)$	[53]
(2)	$e^- + Ar \rightarrow 2e^- + Ar^+$	Electron-impact ionization	$\sigma(E)$	[54]
(3)	$e^- + Ar \rightarrow e^- + Ar_m^*$	Electron-impact excitation	$\sigma(E)$	[55]
(4)	$e^- + Ar \rightarrow e^- + Ar^*$	Electron-impact excitation	$\sigma(E)$	[56]
(5)	$e^- + Ar_m^* \rightarrow 2e^- + Ar^+$	Electron-impact ionization	$\sigma(E)$	[57]
(6)	$e^- + Ar_m^* \rightarrow e^- + Ar^*$	Electron-impact excitation	$\sigma(E)$	[58]
(7)	$e^- + Ti \rightarrow 2e^- + Ti^+$	Electron-impact ionization	$\sigma(E)$	[59]
(8)	$e^- + O_2 \rightarrow 2e^- + O_2^+$	Electron-impact ionization	$\sigma(E)$	[60, 61]
(9)	$e^- + O_2 \rightarrow e^- + O_2^*(a)$	Electron-impact excitation to $a^1\Delta_g$	$\sigma(E)$	[60]
(10)	$e^- + O_2 \rightarrow e^- + O_2^*(b)$	Electron-impact excitation to $b^1\Sigma_g^+$	$\sigma(E)$	[60]
(11)	$e^- + O_2 \rightarrow O^- + O$	Dissociative attachment	$\sigma(E)$	[60]
(12)	$e^- + O_2 \rightarrow e^- + O^- + O^+$	Ion pair formation	$\sigma(E)$	[33]
(13)	$e^- + O_2 \rightarrow 2e^- + O^+ + O$	Dissociative ionization	$\sigma(E)$	[60]
(14)	$e^- + O_2 \rightarrow e^- + O + O$	Dissociation	$\sigma(E)$	[60]
(15)	$e^- + O_2^+ \rightarrow O + O$	Dissociative recombination	$k = 2 \times 10^{-13}(300/T_e)$	[62, 63]
(16)	$e^- + O^+ + O_2 \rightarrow O + O_2$	Recombination	$k = 6 \times 10^{-39}(300/T_e)^{1.5}$*	[63]
(17)	$e^- + O^- \rightarrow 2e^- + O$	Neutralization	$k = 1.95 \times 10^{-18}(T_{gas}/298)^{0.6}$	[64]
Ar^+ collisions				
(18)	$Ar^+ + Ar \rightarrow Ar^+ + Ar$	Elastic scattering	$\sigma(E)$	[65]
(19)	$Ar^+ + Ar \rightarrow Ar + Ar^+$	Charge transfer	$\sigma(E)$	[65]
(20)	$Ar^+ + Ar \rightarrow 2Ar^+ + e^-$	Ion-impact ionization	$\sigma(E)$	[66]
(21)	$Ar^+ + Ar \rightarrow Ar^+ + Ar_m^*$	Ion-impact excitation	$\sigma(E)$	[66]
(22)	$Ar^+ + Ti \rightarrow Ar + Ti^+$	Charge transfer	$k = 6.61 \times 10^{-17}$	[67]
(23)	$Ar^+ + O_2 \rightarrow Ar^+ + O_2$	Elastic scattering	$\sigma(E)$ LH	[33]
(24)	$Ar^+ + O_2 \rightarrow Ar + O_2^+$	Charge transfer	$k = 5.1 \times 10^{-17}$	[68]
(25)	$Ar^+ + O \rightarrow Ar^+ + O$	Elastic scattering	$\sigma(E)$ LH	
(26)	$Ar^+ + O \rightarrow Ar + O^+$	Charge transfer	$k = 6.4 \times 10^{-18}$	[68]
Ar_m^* collisions				
(27)	$Ar_m^* + Ar_m^* \rightarrow Ar + Ar^+ + e^-$	Metastable-metastable collision	$k = 6.4 \times 10^{-16}$	[69, 70]
(28)	$Ar_m^* + Ti \rightarrow Ar + Ti^+ + e^-$	Penning ionization	$\sigma = 4.93 \times 10^{-19}$	[71]
(29)	$Ar_m^* + Ar \rightarrow Ar + Ar$	Two-body collision	$k = 2.3 \times 10^{-21}$	[72]
Ar_f collisions				
(30)	$Ar_f + Ar \rightarrow Ar_{(f)} + Ar_{(f)}$	Elastic scattering	$\sigma(E)$	[73]
(31)	$Ar_f + Ar \rightarrow Ar + Ar^+$	Atom-impact ionization	$\sigma(E)$	[66]
(32)	$Ar_f + Ar \rightarrow Ar_f + Ar_m^*$	Atom-impact excitation	$\sigma(E)$	[74]
Ti^+ collisions				
(33)	$Ti^+ + Ar \rightarrow Ti^+ + Ar$	Elastic scattering	$\sigma = 6 \times 10^{-20}$	[75]
(34)	$Ti^+ + O_2 \rightarrow Ti^+ + O_2$	Elastic scattering	$\sigma(E)$	LH
(35)	$Ti^+ + O \rightarrow Ti^+ + O$	Elastic scattering	$\sigma(E)$	LH

Table 1. Continued.

Ti collisions			
(36) $Ti_f + Ar \rightarrow Ti + Ar_f$	Elastic scattering	$\sigma = 6 \times 10^{-20}$	[75]
(37) $Ti + 2O \rightarrow TiO_2$	Attachment	Only at the walls (SC)	
O^+ collisions			
(38) $O^+ + Ar \rightarrow O^+ + Ar_f$	Elastic scattering	$\sigma(E)$ LH	[33]
(39) $O^+ + Ar \rightarrow O + Ar^+$	Charge transfer	$k = 3 \times 10^{-17}$	(a)
(40) $O^+ + O_2 \rightarrow O^+ + O_2$	Elastic scattering	$\sigma(E)$ LH	[33]
(41) $O^+ + O_2 \rightarrow O + O_2^+$	Charge transfer	$k = 3.3 \times 10^{-17} e^{-0.00169.T_{gas}}$	[62, 63]
(42) $O^+ + O_3 \rightarrow O_2^+ + O_2$	Atom transfer	$k = 1 \times 10^{-16}$	[63]
O_2^+ collisions			
(43) $O_2^+ + Ar \rightarrow O_2^+ + Ar$	Elastic scattering	$\sigma(E)$	LH
(44) $O_2^+ + Ar \rightarrow O_2 + Ar^+$	Charge transfer	$k = 3 \times 10^{-17}$	(a)
(45) $O_2^+ + O_2 \rightarrow O_2^+ + O_2$	Elastic scattering	$\sigma(E)$	LH
(46) $O_2^+ + O_2 \rightarrow O_2 + O_2^+$	Charge transfer	$k = 3 \times 10^{-17}$	(a)
O^- collisions			
(47) $O^- + Ar \rightarrow O^- + Ar$	Elastic scattering	$\sigma(E)$ LH	[33]
(48) $O^- + O_2 \rightarrow O^- + O_2$	Elastic scattering	$\sigma(E)$ LH	[33]
(49) $O^- + O_2 \rightarrow e^- + O_3$	Recombination	$k = 5 \times 10^{-21}$	[63]
(50) $O^- + O_2(a) \rightarrow e^- + O_3$	Recombination	$k = 3 \times 10^{-16}$	[62, 63]
(51) $O^- + O_2(b) \rightarrow e^- + O + O_2$	Recombination	$k = 6.9 \times 10^{-16}$	[62, 63]
(52) $O^- + O \rightarrow e^- + O_2$	Recombination	$k = 5 \times 10^{-16}$	[63]
(53) $O^- + O^+ \rightarrow O + O$	Recombination	$k = 2 \times 10^{-13}(300/T_{gas})^{0.5}$	[63]
(54) $O^- + O_2^+ \rightarrow O + O + O$	Recombination	$k = 1 \times 10^{-13}$	[63]
(55) $O^- + O_2^+ \rightarrow O + O_2$	Recombination	$k = 2 \times 10^{-13}(300/T_{gas})^{0.5}$	[63]

albeit, as neutral particles. Moreover, the metastable Ar_m^* atoms are reflected as ground state Ar atoms. In other words, the reactor walls act as a loss mechanism for Ar^+ ions, Ar_m^* metastable atoms, Ti^+ ions, O^+ ions, O_2^+ ions and O^- ions. In contrast to the above-mentioned species, Ti and O atoms, and O_2 molecules do have a certain probability to interact with a wall, i.e. the sticking probability, or SC, is not zero. In the low pressure case that we investigate, the SC does not have a large impact on the corresponding particle densities. Therefore, on the walls, excluding the substrate, a constant SC is assumed, i.e. 0.5 for Ti [42], 1 for O [5] and 0 for O_2. However, to describe the deposition process of the TiO_x film on the substrate, and to predict its stoichiometry, some effective sticking coefficients, SC_{eff}, of Ti, O and O_2 need to be calculated. These SC_{eff} values are not constant, but are influenced by the incorporation or coverage of the different implanted or adsorbed species on the surface, respectively [5]. Therefore, an analytical surface model, based on the models described in [16, 17, 43] is coupled to the PIC/MCC model, in order to account for this effect of changing SC upon surface coverage by compound material. The general compound fraction balance equation for the deposition of O_2 (giving rise to two deposited O species), O and Ti on the substrate to form a TiO_x film with a desired stoichiometry x is [16, 17, 43]

$$\frac{2}{x}SC_{O_2}F_{O_2}^{t,r}(1 - \theta_{cs}^{t,r}) + \frac{1}{x}SC_O F_O^{t,r}(1 - \theta_{cs}^{t,r}) = SC_{Ti}F_{Ti}^{t,r}\theta_{cs}^{t,r}. \tag{6}$$

Note that we use the static description of the analytical surface model. This means that $\theta_{cs}^{t,r}$ is not calculated with its value from the previous time step, i.e. $d\theta_{cs}^{t,r}/dt = 0$. The time dependence arises from the PIC fluxes, $F^{t,r}$, which are calculated as a function of time.

Since the desired stoichiometry x of the TiO$_x$ film is two, the surface model needs to account for this. Therefore, the compound fraction balance equation, for the deposition of a TiO$_x$ film with stoichiometry $x = 2$, is

$$SC_{O_2}F_{O_2}^{t,r}(1-\theta_{cs}^{t,r}) + \tfrac{1}{2}SC_O F_O^{t,r}(1-\theta_{cs}^{t,r}) = SC_{Ti}F_{Ti}^{t,r}\theta_{cs}^{t,r}. \tag{7}$$

With this equation, at every PIC/MCC time step (t), the compound (c) fraction on every radial position (r) on the substrate (s), i.e. $\theta_{cs}^{t,r}$, is derived from the fluxes (F) of the incoming O$_2$, O and Ti species (calculated with the PIC/MCC model), with corresponding constant SC, which are chosen as 0.3 for O$_2$ [5], 1 for O [5] and 0.5 for Ti [42]:

$$\theta_{cs}^{t,r} = \frac{SC_{O_2}F_{O_2}^{t,r} + \tfrac{1}{2}SC_O F_O^{t,r}}{SC_{O_2}F_{O_2}^{t,r} + \tfrac{1}{2}SC_O F_O^{t,r} + SC_{Ti}F_{Ti}^{t,r}}. \tag{8}$$

Subsequently, the SC values of O and O$_2$ are adapted at that time step by the compound fraction, $\theta_{cs}^{t,r}$, so that we obtain the so-called effective sticking coefficients, SC$_{eff}$, for this time step, on every position r on the substrate:

$$SC_{O_2,eff}^{t,r} = SC_{O_2}(1-\theta_{cs}^{t,r}),$$
$$SC_{O,eff}^{t,r} = SC_O(1-\theta_{cs}^{t,r}). \tag{9}$$

Indeed, the sticking of O and O$_2$ on TiO$_x$ compound will be lower than on a pure metallic surface. Since the sticking of Ti is independent of the compound fraction (i.e. Ti will stick in a similar way on a metallic Ti surface and on a TiO$_x$ surface), a constant SC$_{Ti}$ can be used, i.e. $SC_{Ti,eff}^{t,r} = SC_{Ti}$. Note that the actual stoichiometry of the deposited TiO$_x$ film at steady state, $x^{t,r}$, is found by multiplying the desired stoichiometry, $x = 2$, with the compound fraction, $\theta_{cs}^{t,r}$.

When an SP is created or reflected at a wall, the direction of its velocity is chosen as such to obey the cosine law [44]. As a consequence, the azimuthal angle, $\phi = 2\pi.\text{RN}[0,1]$, whereas the polar angle, $\theta = \sin^{-1}(\sqrt{\text{RN}[0,1]})$. RN[0, 1] is a random number uniformly distributed in the interval [0, 1]. For emission of an electron from the cathode surface, the components of the velocity vector $\mathbf{v}$, v_r and v_θ are correspondent to the azimuthal angle, ϕ, whereas v_z is derived from the polar angle, θ. In cylindrical coordinates, this becomes:

$$v_r = v_x \cos(2\pi.\text{RN}[0,1]) + v_y \sin(2\pi.\text{RN}[0,1]),$$
$$v_\theta = -v_x \sin(2\pi.\text{RN}[0,1]) + v_y \cos(2\pi.\text{RN}[0,1]), \tag{10}$$
$$v_z = v_0\sqrt{\text{RN}[0,1]}.$$

When this created or reflected SP is an electron, its energy is assumed as 4 eV. When the SP is another species, its energy depends on the thermal accommodation coefficient, α:

$$\alpha = \frac{E_i - E_r}{E_i - E_w}, \tag{11}$$

where E_i is the mean energy of the incoming particles, E_r is the mean energy of the reflected particles and E_w is the mean energy of the reflected particles in thermal equilibrium with the wall ($2kT_w$). In our simulation, α is assumed as 0.5 [45], and a random number between 0 and 1

is generated. When the random number is lower than α, an inelastic reflection occurs, and if the random number is higher than α, an elastic reflection occurs. After an inelastic reflection, the particle is thermalized and removed from the calculation (unless in the case of a reflected Ti or O atom, which is described with diffusion equations, see below). On the other hand, if the particle is elastically reflected, its energy is conserved. The direction of the velocity is chosen as such to obey the cosine law [44], and its components (v_r, v_θ, v_z) are as in equation (10).

Also, the effects of poisoning on the plasma–target interactions, i.e. on the SEEC and on the sputter yield, is included in the model. In the present work, we used O_2 gas flows for which the target is completely in the poisoned mode, in order to avoid (i) the simulation of the hysteresis and (ii) having to deal with a partially reacted Ti target. However, due to the target surface modification the SEEC is altered, which results in a target voltage change [46]. In the model, the poisoning of the target is therefore described by changing the SEEC value, depending on the O_2 gas pressure, and in correspondence to the range reported in [46]. As far as sputtering is concerned, both Ti and O atoms can be sputtered from a poisoned target, but with a lower sputter yield than for a metallic Ti target. Therefore, in the model, the sputter yield, calculated with the formula of Matsunami *et al* [41], is lowered by a factor, in accordance to the values reported in [47]: the sputter yield of Ti from a fully poisoned TiO_x target is lowered by a factor of 8.8 compared to the sputter yield of Ti from a metallic target, and the sputter yield of O from a poisoned target is two times higher, compared to the sputter yield of Ti from a fully poisoned target [47].

When treating the slow (thermalized) particles with the PIC/MCC method, the computation time would be tremendously high to reach a steady state. Therefore, alternative methods are used, according to the species' physical behavior. The neutral slow particles can be subdivided into motionless and diffusing species. In the plasma, the motionless background gas atoms or molecules (Ar and O_2) are initially slow, but can be heated [48]. The partial pressure of the gases, p_{Ar} and p_{O_2} is kept constant in each simulation. Thermalization of fast atoms by collisions with background gas atoms or molecules can cause the background gases to heat up, i.e. the temperatures, T_{Ar} and T_{O_2} will increase. The densities of the gases, n_{Ar} and n_{O_2}, which change due to gas heating, can be calculated at every position and at every time step, with the ideal gas law:

$$n = \frac{p}{k_B T}. \tag{12}$$

Here, k_B is the Boltzmann constant. The flux of O_2 is needed to picture the deposition of the TiO_x film. The flux is calculated as the amount of collisions with a surface per second:

$$F = \tfrac{1}{4} n v. \tag{13}$$

The velocity, v, is the average velocity of the gas molecules, i.e. thermal velocity $v = \sqrt{\frac{2k_B T}{m}}$. The diffusing atoms can be created as slow particles, or can be slowed down by collisions (Ti and O). Their density $n_{slow}(r, z)$ is calculated with the diffusion equation:

$$\frac{\partial n_{slow}}{\partial t} - D\Delta n_{slow}(r, z) = r_{prod}(r, z) - r_{loss}(r, z), \tag{14}$$

where D is the diffusion coefficient of Ti or O atoms in Ar gas, and r_{prod} and r_{loss} are the production and loss rates. The production of a slow Ti or O atom (r_{prod}) can be caused by thermalization of a fast Ti or O atom, or direct creation of a slow Ti or O atom. The loss of a
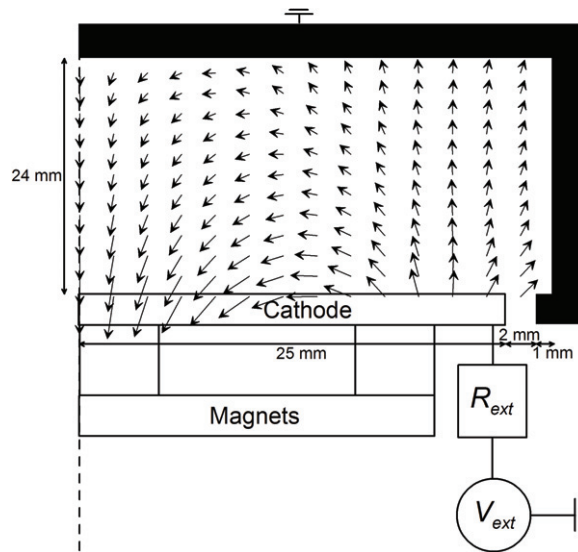
Figure 2. Scheme of the simulated two-dimensional magnetron area, with the external electrical circuit generating an electric field, and the external magnets, creating a magnetic field (magnetic field vectors are indicated on the figure). The cylindrical three-dimensional magnetron discharge is apparent by rotating around the dashed symmetry axis.

slow Ti or O atom (r_{loss}) can be due to heating of a slow Ti or O atom. The diffusion coefficients D (in $m^2\,s^{-1}$) are calculated from the rigid sphere approximation [49]:

$$D = 2.628 \times 10^{-7} \frac{\sqrt{T^3 \left(M_1 + M_2\right)/2M_1M_2}}{p d_{12}^2}, \qquad (15)$$

where T is the gas temperature (K), M_1 and M_2 are the masses of Ti (or O) and Ar (g/mole), p is the pressure (atm) and d_{12} is the collision diameter (10^{-10} m), given by $\frac{(d_1+d_2)}{2}$. The collision diameter of Ti is 2.684×10^{-10} m [50], 3.050×10^{-10} m for O [51] and 3.542×10^{-10} m for Ar [51].

3. Results and discussion

3.1. General conditions

The simulations are performed for a planar circular magnetron with a 25 mm radius Ti target, installed in a cylindrical chamber. The magnetron discharge operates at room temperature (300 K). The axisymmetric magnetic field has a maximum radial strength of 1040 Gauss, and is schematically presented in figure 2. Due to the cylindrical symmetry of the reactor, the simulations can be carried out in 2d (r,z): the simulation area is presented in figure 2.

An electrical circuit, consisting of an external resistance ($R_{\text{ext}} = 1500\,\Omega$) and voltage source ($V_{\text{ext}} = -600\,V$), is connected to the cathode, whereas the other walls are grounded, to generate an electric field. The coupling of the external circuit to the PIC/MCC code is explained in [34].
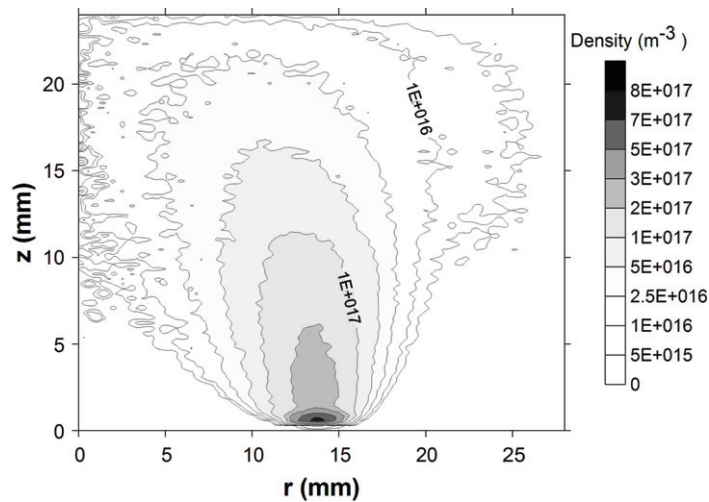
Figure 3. Calculated electron density profile (in m^{-3}) at an Ar partial pressure of 1.0 Pa and an O_2 partial pressures of 0.12 Pa. Note that the Y-axis ($r = 0$) corresponds to the symmetry axis of the cylindrically symmetrical reactor.

In order to study the effect of the O_2/Ar gas ratio, the Ar partial pressure was kept constant at 1 Pa for all the calculations, while the partial pressure of O_2 was varied as 0.02, 0.06, 0.12, 0.18 and 0.24 Pa, according to measured values. The calculated currents and voltages at the different O_2/Ar gas proportions are in the range of 0.18–0.2 A and 310–330 V, respectively. The values correspond well with experimental values at similar conditions [52].

3.2. Potential distribution, and charged species density profiles

Light-weighted electrons have the highest mobility from all the species in the discharge. Therefore, they are rapidly lost to the reactor walls, while the (mainly positive) ions remain in the discharge. As a consequence, the walls charge negatively, leaving behind a positively charged 'sheath' area. This transition area between the bulk plasma and the wall is characterized by a decreasing potential from the bulk to the wall (by equation (2)). This causes positive ions to reside in the sheath and negative ions to reside in the positive potential part of the plasma, i.e. the bulk (see below). When a negative potential is applied to the cathode, the sheath in front of the cathode is the most distinct. Indeed, the whole potential difference is passed through in this small area. As a result, the positive ions which enter the cathode sheath are accelerated to the cathode target. When an external magnetic field is present, electrons are confined to the magnetic field lines, leading to a higher electron density at the maximum radial magnetic field, as presented in figure 3 (for the case of 0.12 Pa O_2). The electron density is only weakly dependent on the O_2/Ar proportion.

The electrons ionize neutral Ar, O_2, O and Ti species, causing the positive ion density to be highest in the same area. All have similar profiles as the electron density so they are not shown here. The Ar^+ density has approximately the same magnitude as the electron density, the O^+ and O_2^+ densities are two orders of magnitude lower (the latter is shown in figure 4), and the Ti^+ density is three orders of magnitude lower. Both the Ar^+ and the Ti^+ density do not change much with O_2/Ar ratio. However, the O^+ and O_2^+ densities rise with O_2 gas pressure, as is clear
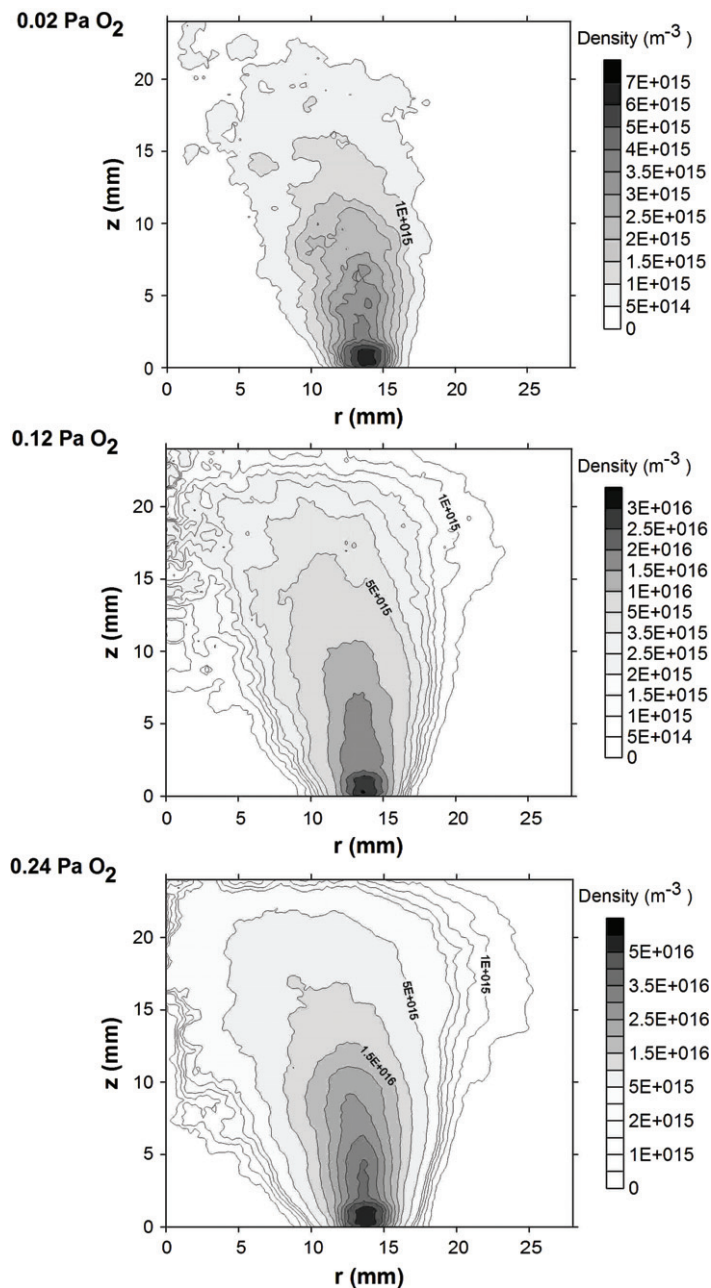
Figure 4. Calculated O_2^+ density profiles (in m^{-3}) at an Ar partial pressure of $1.0\,Pa$ and O_2 partial pressures of 0.02, 0.12 and 0.24 Pa. Note that the Y-axis ($r = 0$) corresponds to the symmetry axis of the cylindrically symmetrical reactor.

from figure 4. The total positive ion density profile causes the sheath to be thinnest where the density is at maximum, i.e. at a radial position of 13.5 mm, as a consequence of decreasing Debye length at increasing ion density.

The charged particles' distribution generates an electric potential distribution, and together with the externally applied potential, a typical plasma potential distribution is created, as shown in figure 5. A steep ascend from cathode to bulk over the sheath area is observed, becoming flat
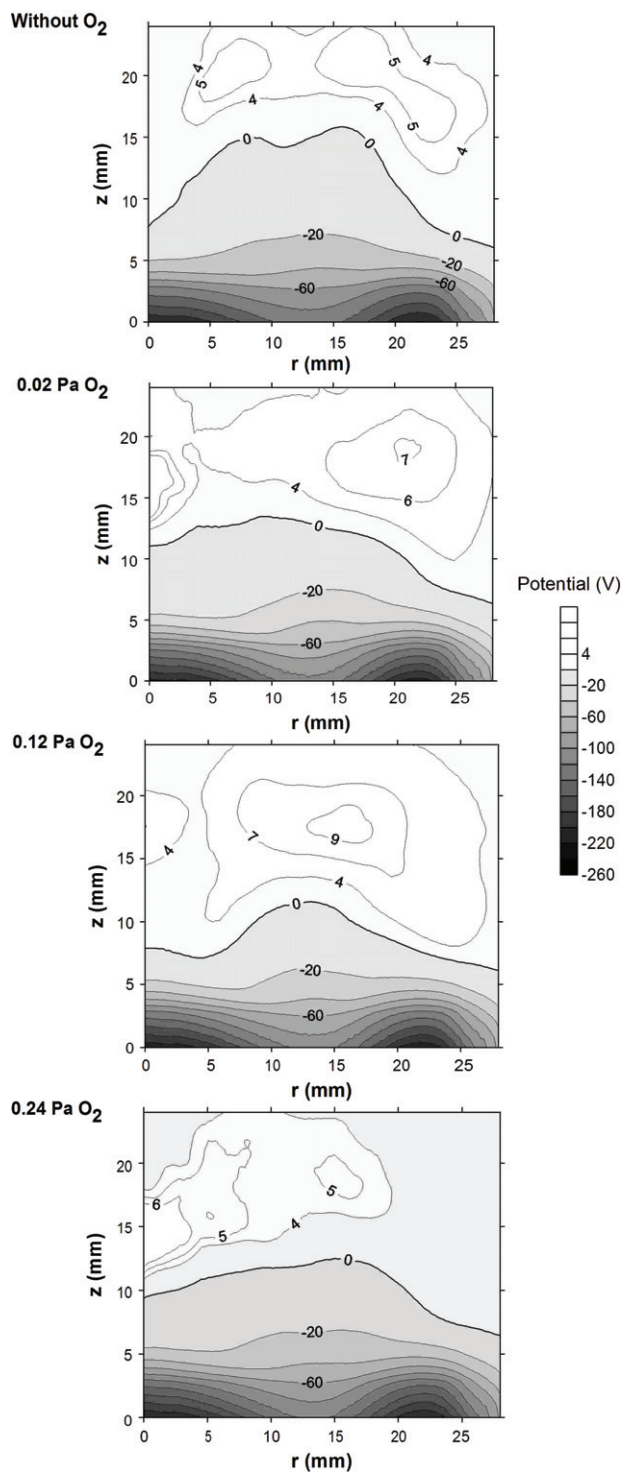
IOP Institute of Physics **Φ** DEUTSCHE PHYSIKALISCHE GESELLSCHAFT

Figure 5. Calculated plasma potential distribution at an Ar partial pressure of 1.0 Pa, without O_2 and at O_2 partial pressures of 0.02, 0.12 and 0.24 Pa. Note that the Y-axis ($r = 0$) corresponds to the symmetry axis of the cylindrically symmetrical reactor. The line that separates the negative and positive potential area ($V = 0$) is marked thicker for clarity.

and positive in the bulk, and decreasing to zero toward the grounded anode walls. Due to the external magnetic field, the plasma potential well is steeper and the sheath is thinner at the area where the radial magnetic field is at maximum, as is clear from figure 5.

When no O_2 gas is present, the negative space charge is only created by electrons, which are confined to the magnetic field in an area close to the cathode. As a result, the positive area of the electric potential is only found in a narrow area close to the grounded reactor walls, as is clear from figure 5 (top figure).

When O_2 is added to the Ar gas, negative O^- ions are created by the electron impact reactions (11) and (12) from table 1. Because the electrons are confined to the magnetic field in an area close to the cathode, the O^- ions are also created in this area. However, taking into account that heavy O^- ions are not trapped in the magnetic field in contrast to electrons, the plasma potential distribution (figure 5) forces the negative O^- ions to move towards the positive potential area. Figure 6 presents the calculated O^- density, which has a maximum at the positive potential area. This negative ion density causes the positive potential area to enlarge, see figure 5 (compare 'without O_2' with '0.02 Pa O_2').

Figure 5 also illustrates that at increasing O_2 density, the positive potential area moves toward the symmetry axis of the magnetron. This is also true for the O^- density (see figure 6), which also becomes smaller and more spread out. The decreasing trend of the O^- density is a bit unexpected, but it is a consequence of the O^+ and O_2^+ densities, which rise significantly when the O_2 pressure is increased, as was clear from figure 4 above. Consequently, the recombination reactions (53), (54) and (55) from table 1 occur much more often, which are an important loss mechanism for O^- ions. Therefore, the O^- density decreases upon O_2 addition (see figure 6). When the density drops, the Debye length increases leading to a less pronounced O^- shielding of the anode potential. This results in a spreading of the density profile and a spreading of the positive potential area toward the center of the discharge.

3.3. Calculated sputtered Ti and O fluxes

The plasma species can bombard the target surface and sputter Ti and O atoms. Positive Ar^+, Ti^+, O^+ and O_2^+ ions, and fast Ar_f atoms contribute to the sputtering of the poisoned TiO_x target. The sputtered Ti and O fluxes at different values of the O_2 partial pressure are presented in figure 7. The sputtered Ti flux in the case of a pure Ar discharge is not presented here. It is around 10 times higher than the obtained valued in the O_2/Ar mixture as a consequence of the lower sputter yield when the target is poisoned. As a consequence of localized bombardment of plasma species to the target, the sputtered Ti and O fluxes exhibit a peak profile. This localized sputtering causes the typical eroded race-track area in the target.

The sputtered Ti and O fluxes are approximately equal, although the sputter yield of O is two times higher than of Ti (see section 2). This is caused by the fact that the threshold energy for sputtering Ti by Ar^+ ions is lower (the main sputter source in the discharge) than sputtering O by Ar^+ ions (the threshold energy for sputtering Ti with Ar^+ ions is 12.55 eV and 18.85 eV for sputtering O). Also, there is no dependence of the amount of sputtering on the O_2 partial pressure, since most sputtering is caused by Ar^+ ions, which flux is independent of the O_2 partial pressure.
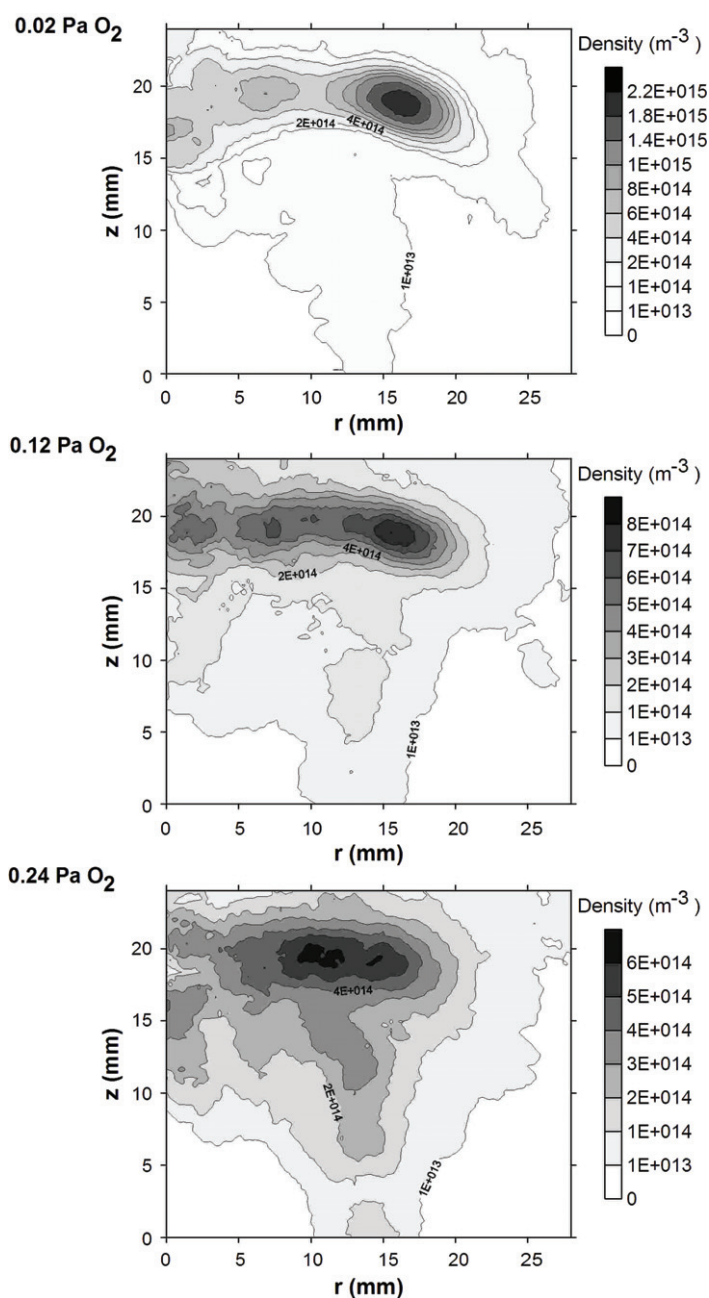
Figure 6. Calculated O⁻ density profiles (in m⁻³) at an Ar partial pressure of 1.0 Pa and O₂ partial pressures of 0.02, 0.12 and 0.24 Pa. Note that the Y-axis ($r = 0$) corresponds to the symmetry axis of the cylindrically symmetrical reactor.

3.4. Calculated Ti, O and O₂ fluxes to the substrate

The sputtered Ti and O atoms, together with the produced O atoms by plasma reactions, as well as the O₂ gas molecules, move through the plasma and can be deposited on a substrate, placed in front of the target. The calculated Ti, O and O₂ fluxes to the substrate are shown in figure 8.
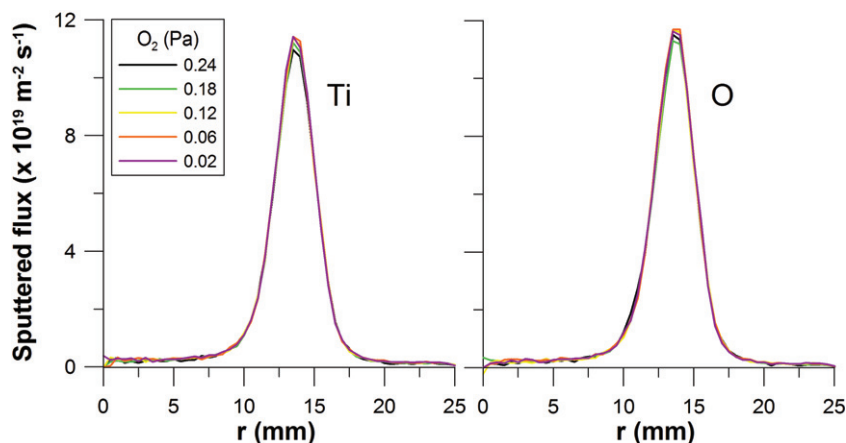
Figure 7. Calculated sputtered Ti and O fluxes from the cathode for different O_2 partial pressures as indicated in the legend, and at an Ar partial pressure of 1.0 Pa. Note that the Y-axis ($r = 0$) corresponds to the symmetry axis of the cylindrically symmetrical reactor.
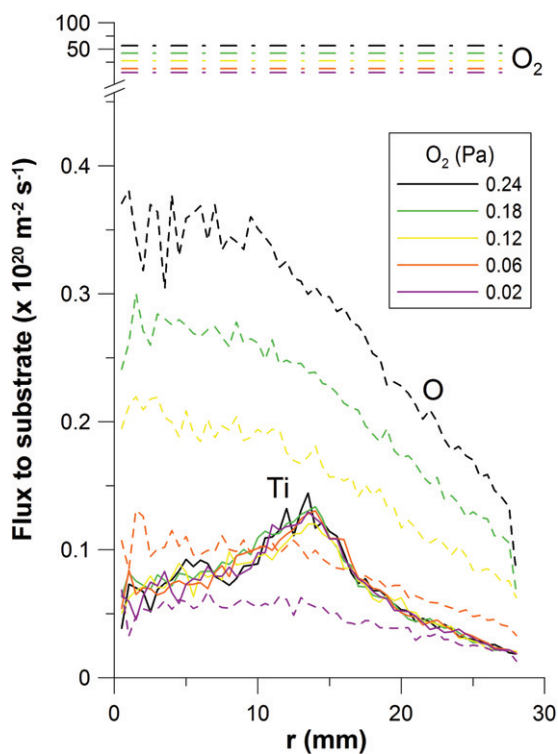

Figure 8. Calculated fluxes of the Ti, O and O_2 species to the substrate, as a function of radial position, for different O_2 partial pressures, at an Ar partial pressure of 1 Pa. The value $r = 0$ corresponds to the symmetry axis of the cylindrically symmetrical reactor.

O^+, O_2^+ and O^- ions are also present close to the substrate (see figures 4 and 6). However, their flux to the substrate is several orders of magnitude lower than the O flux, causing these ions to have a negligible contribution to the deposition of the TiO_x film.
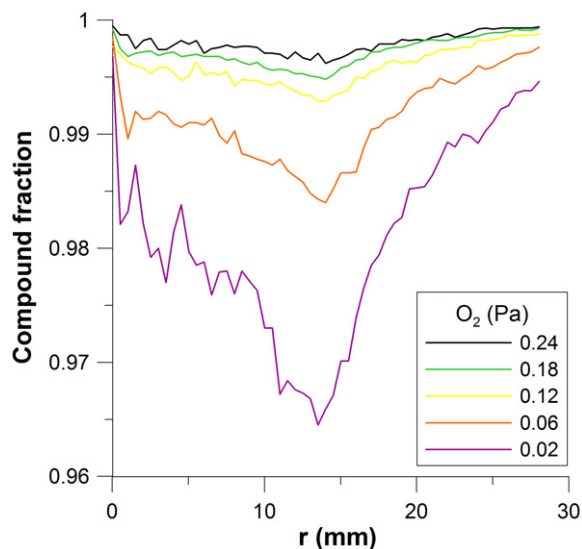
Figure 9. Calculated compound fraction on the substrate surface, as a function of radial position, for different O_2 partial pressures, at an Ar partial pressure of 1 Pa. The value $r = 0$ corresponds to the symmetry axis of the cylindrically symmetrical reactor.

The Ti flux to the anode has a peak profile caused by the sputtered Ti peak profile (see figure 7). This will cause the deposited Ti in the film to be non-uniform. However, the peak is broadened as a consequence of diffusion of the sputtered Ti atoms through the plasma. This means that when the substrate is placed further from the target, the film thickness will become more uniform. The Ti flux to the anode remains virtually constant for increasing O_2 amount, in correspondence to the sputtered Ti flux (see section 3.3 and figure 7 above).

Although the sputtered Ti and O fluxes are equal, the O flux to the anode is almost everywhere higher than the Ti flux. This is caused by the additional production processes of O atoms besides sputtering, i.e. O atoms are also created by plasma reactions. Moreover, the O flux has lost its radial peak profile, caused by O sputtering (see figure 7), because more O atoms are created by plasma reactions than by sputtering. The O flux increases upon O_2 addition, which is a consequence of higher O production at higher O_2 amount.

At the gas pressures under consideration, gas heating is not so important [48]. As a result the Ar and O_2 gas densities remain constant and uniform (see also equation (12)). Consequently, the O_2 flux bombarding the substrate has a uniform spatial profile. Logically, the O_2 flux increases for higher O_2 partial pressure (see also equation (13)).

3.5. Calculated deposition of a TiO_x film on the substrate

Based on these calculated Ti, O and O_2 fluxes (figure 8) and the corresponding SC values, the radial deposited fraction of TiO_x (i.e. the 'compound fraction') on the substrate is calculated with equation (8), and it is presented in figure 9. It is clear that the compound fraction is close to unity for all O_2 partial pressures investigated. The lower compound coverage at a radial position of 13.5 mm is caused by the Ti flux, because both quantities are inversely proportional by equation (8). At increasing O_2 amount, the compound fraction on the substrate increases as a
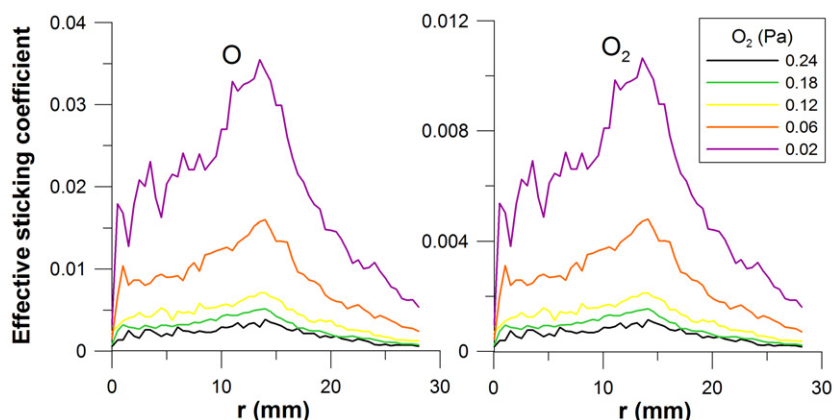
Figure 10. Calculated effective sticking coefficients, SC_{eff}, of O and O_2, as a function of radial position, for different O_2 partial pressures, at an Ar partial pressure of 1 Pa. The value $r = 0$ corresponds to the symmetry axis of the cylindrically symmetrical reactor.

result of the higher O and O_2 fluxes, and it becomes more uniform because these oxygen fluxes gain importance in the compound coverage, and they have a more uniform profile compared to the peaking Ti flux.

Based on this radial compound fraction, the constant SC values of O and O_2 are adapted, according to equation (9). The calculated effective SC values (SC_{eff}) of O and O_2 are presented in figure 10. In contrast to the radially constant SC values of a metallic substrate, the effective SC_{eff} values are not constant in the radial direction. Indeed, the SC_{eff} profile exhibits a radial dependence, being lowest at the highest compound fraction. In comparison with the constant initial SC values of O and O_2, i.e. 1 and 0.3, the effective values have dropped by about a factor of 25–250. Moreover, the effective sticking of the O and O_2 species decreases at increasing O_2 gas pressure, caused by the higher compound fraction.

The deposition rate of Ti and O can be found when multiplying the fluxes of Ti, O and O_2 (figure 8) by the corresponding SC_{eff} values. The total deposition rate of oxygen is the sum of the deposition rates due to O and O_2 (note that O_2 counts double, because one O_2 molecule gives rise to two deposited O atoms). Figure 11 shows that the total deposition rate of O is two times higher than the deposition rate of Ti, which is required to deposit a TiO_2 film. The calculated stoichiometries for three of the investigated O_2 partial pressures are also presented (figure 11: gray curves, right axis). At the lowest O_2 amount (0.02 Pa), the stoichiometry of two is almost achieved (with a minimum value of 1.93). At increasing O_2 amount, the deposition rates of both Ti and O are hardly affected, but nevertheless, the small effect results in a stoichiometry becoming equal to two. The latter could also be predicted by the compound coverage, as was presented in figure 9: the real stoichiometry of the film is found by multiplying the desired stoichiometry $x = 2$ by the compound coverage (note that the desired stoichiometry $x = 2$ was imposed by equation (7)). This means that an O_2/Ar proportion of 1/10 is already enough to deposit a stoichiometric film (with a minimum value of 1.98), with a satisfactory deposition rate.

The peak profiles in figure 11 for the total deposition rates of Ti and O illustrate that the deposited film will have a non-uniform thickness, under the investigated conditions. This
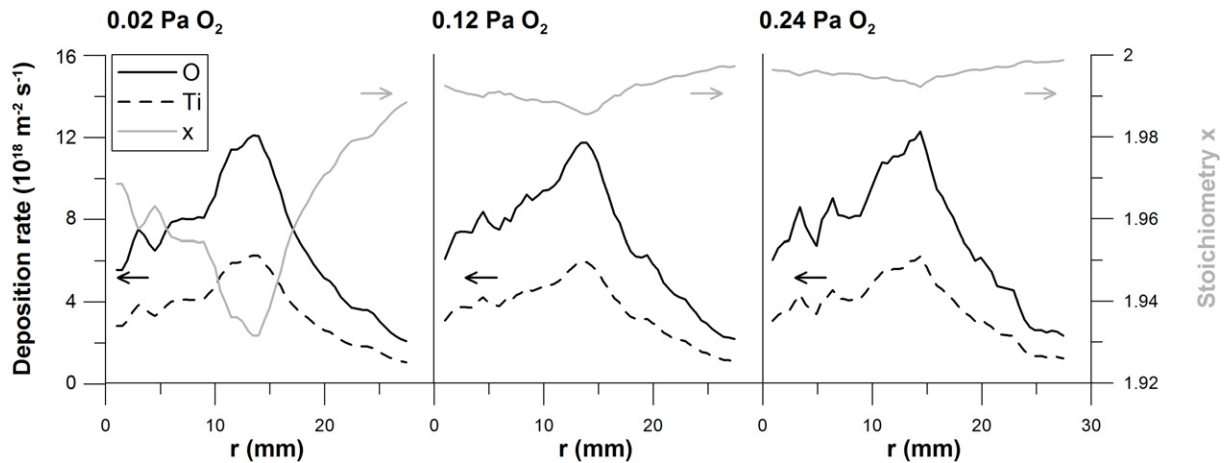
Figure 11. Calculated deposition rate of Ti and total O as a function of radial position (black curves, left axis) at an Ar partial pressure of 1 Pa and O_2 partial pressures of 0.02, 0.12 and 0.24 Pa. Also shown is the calculated stoichiometry x of the deposited TiO_x films (gray curves, right axis). The value $r = 0$ corresponds to the symmetry axis of the cylindrically symmetrical reactor.

is caused by the non-uniform Ti flux (figure 8) leading to radially dependent SC_{eff} values (figure 10). It is expected that a more uniform film can be deposited by placing the substrate further from the target so that the fluxes to the substrate are smoothed out. It was also found that O_2 contributes at least 50 times more than O to the total deposition of oxygen in the TiO_x film. This is caused by the much higher O_2 flux compared to the O flux (see figure 8 above), although the SC_{eff} of O_2 is lower than that of O (see figure 10 above).

4. Conclusion

A 2d3v PIC/MCC model was developed to investigate the physical processes in a magnetron discharge during the reactive sputter deposition of TiO_x films. The plasma species taken into account are electrons, Ar^+ ions, fast Ar_f atoms, metastable Ar_m^* atoms, Ti^+ ions, Ti atoms, O^+ ions, O_2^+ ions, O^- ions and O atoms. This model includes target sputtering, secondary electron emission, electron reflection, atom sticking and the effects of target poisoning (on sputter yield and SEEC value). To investigate the deposition process of the TiO_x film, an analytical surface model was coupled to the PIC/MCC model. With this combined model, the cathode current and voltage, the plasma potential and electric field distribution, as well as the density profiles and fluxes of the different plasma species are calculated. Also, the stoichiometry x of the TiO_x film and its deposition rate can be obtained in a self-consistent manner.

The plasma characteristics were calculated at different O_2/Ar gas proportions. Note that at the lowest O_2/Ar gas proportion, the target is already completely poisoned. It was shown that at constant Ar partial pressure, higher O_2 pressures cause higher O^+ and O_2^+ densities. This leads to enhanced recombination reactions of these ions with the negative O^- ions, causing their density to become smaller, and more spread out. This also results in a more spread out positive plasma potential toward the center of the reactor.

The deposition of the TiO_x film was investigated, and it was calculated that at the O_2/Ar gas proportions under study, the stoichiometry of $x = 2$ is almost achieved. When increasing the O_2/Ar gas proportion, the stoichiometry rises to exactly $x = 2$, whereas the deposition rates of both Ti and O are hardly affected. The deposited O in the TiO_x film originates almost entirely from the O_2 gas: O_2 molecules contribute at least 50 times more to the total oxygen deposition than O atoms.

Acknowledgments

References

[1] Bradley J W, Thompson S and Gonzalvo Y A 2001 Measurement of the plasma potential in a magnetron discharge and the prediction of the electron drift speeds *Plasma Sources Sci. Technol.* **10** 490

[2] Safi I 2000 A novel reactive magnetron sputtering technique for producing insulating oxides of metal alloys and other compound thin films *Surf. Coat. Technol.* **135** 48

[3] Koski K, Holsa J, Juliet P, Wang Z H, Aimo R and Pischow K 1999 Characterisation of aluminium oxide thin films deposited on polycarbonate substrates by reactive magnetron sputtering *Mater. Sci. Eng.* B **65** 94

[4] Ghekiere P, Mahieu S, De Winter G, De Gryse R and Depla D 2005 Scanning electron microscopy study of the growth mechanism of biaxially aligned magnesium oxide layers grown by unbalanced magnetron sputtering *Thin Solid Films* **493** 129

[5] Möller W and Güttler D 2007 Modelling of plasma-target interaction during reactive magnetron sputtering of TiN *J. Appl. Phys.* **102** 094501

[6] Depla D and De Gryse R 2001 Influence of oxygen addition on the target voltage during reactive sputtering of aluminium *Plasma Sources Sci. Technol.* **10** 547

[7] Depla D, Tomaszewski H, Buyle G and De Gryse R 2006 Influence of the target composition on the discharge voltage during magnetron sputtering *Surf. Coat. Technol.* **201** 848

[8] Depla D and Mahieu S 2008 *Reactive Sputter Deposition* (Berlin: Springer)

[9] Pekker L and Krasheninnikov S I 2000 On the theory of low-pressure magnetron glow discharge *Phys. Plasmas* **7** 382

[10] Lan Gu and Lieberman M A 1988 Axial distribution of optical emission in a planar magnetron discharge *J. Vac. Sci. Technol.* A **6** 2960

[11] Bradley J W, Arnell R D and Armour D G 1997 Measurement and modelling of the bulk plasma in magnetron sputtering sources *Surf. Coat. Technol.* **97** 538

[12] Bradley J W, Thompson S and Gonzalvo Y A 2001 Measurement of the plasma potential in a magnetron discharge and the prediction of the electron drift speeds *J. Phys. D: Appl. Phys.* **34** 3241

[13] Wendt A E and Lieberman M A 1990 Spatial structure of a planar magnetron discharge *J. Vac. Sci. Technol.* A **8** 902

[14] Buyle G 2005 Simplified model for the planar DC magnetron discharge *PhD Thesis* Ghent University

[15] Buyle G, Depla D, Eufinger K, Haemers J, De Bosscher W and De Gryse G 2004 Simplified model for the dc planar magnetron discharge *Vacuum* **74** 353

[16] Berg S and Nyberg T 2005 Fundamental understanding and modeling of reactive sputtering processes *Thin Solid Films* **476** 215

IOP Institute of Physics Φ DEUTSCHE PHYSIKALISCHE GESELLSCHAFT

[17] Depla D, Heirwegh S, Mahieu S and De Gryse R 2007 Towards a more complete model for reactive magnetron sputtering *J. Phys. D: Appl. Phys.* **40** 1957

[18] Kolev I and Bogaerts A 2004 Numerical models of the planar magnetron glow discharges *Contrib. Plasma. Phys.* **44** 582

[19] Bradley J W 1996 The plamsa properties adjacant to the target in a magnetron sputtering source *Plasma Sources Sci. Technol.* **5** 622

[20] Costin C, Marques L, Popa G and Gousset G 2005 Two-dimensional fluid approach to the dc magnetron discharge *Plasma Sources Sci. Technol.* **14** 168

[21] Bogaerts A, Van Straaten M and Gijbels R 1995 Description of the thermalisation process of the sputtered atoms in a glow discharge using a three-dimensional Monte Carlo method *J. Appl. Phys.* **77** 1868

[22] Birdsall C K and Langdon A B 1991 *Plasma Physics via Computer Simulations* (Bristol: IOP Publishing)

[23] Kolev I and Bogaerts A 2006 Detailed numerical investigation of a dc sputter magnetron *IEEE Trans. Plasma Sci.* **34** 886

[24] Kolev I and Bogaerts A 2006 PIC/MCC numerical simulation of a dc planar magnetron *Plasma Process. Polym.* **3** 127

[25] Van Aeken K, Mahieu S and Depla D 2008 The metal flux from a rotating cylindrical magnetron: a Monte Carlo simulation *J. Phys. D: Appl. Phys.* **41** 205307

[26] Pflug A, Szyszka B and Niemann J 2003 Simulation of reactive sputtering kinetics in real in-line processing chambers *Thin Solid Films* **442** 21

[27] Nanbu K, Segawa S and Kondo S 1996 Self-consistent particle simulation of three-dimensional dc magnetron discharge *Vacuum* **47** 1013

[28] van der Straaten T A, Cramer N F, Falconer I S and James B W 1998 The cylindrical dc magnetron discharge: I particle-in-cell simulation *J. Phys. D: Appl. Phys.* **31** 177

[29] Kondo S and Nanbu K 1999 A self-consistent numerical analysis of a planar dc magnetron discharge by the particle-in-cell/Monte Carlo method *J. Phys. D: Appl. Phys.* **32** 1142

[30] Shon C H and Lee J K 2002 Modeling of magnetron sputtering plasmas *Appl. Surf. Sci.* **192** 258

[31] Kusumoto Y and Iwata K 2004 Numerical study of the characteristics of erosion in magnetron sputtering *Vacuum* **74** 359

[32] Kolev I, Bogaerts A and Gijbels R 2005 Influence of electron recapture by the cathode upon the discharge characteristics in dc planar magnetrons *Phys. Rev.* E **72** 056402

[33] Nanbu K, Mitsui K and Kondo S 2000 Self-consistent particle modelling of dc magnetron discharges of an O_2/Ar mixture *J. Phys. D: Appl. Phys.* **33** 2274

[34] Bultinck E, Kolev I, Bogaerts A and Depla D 2007 The importance of an external circuit in a particle-in-cell/monte carlo collisions model for a direct current planar magnetron *J. Appl. Phys.* **103** 013309

[35] Bultinck E, Mahieu S, Depla D and Bogaerts A 2009 The reactive sputter deposition of a TiN film, simulated with a particle-in-cell/Monte Carlo collisions model *New J. Phys.* **11** 023039

[36] Nanbu K and Kitatani Y 1995 An ion-neutral collision model for particle simulation of glow discharge *J. Phys. D: Appl. Phys.* **28** 324

[37] Georgieva V, Bogaerts A and Gijbels R 2003 Particle-in-cell/Monte Carlo simulation of a capacitively coupled radio frequency Ar/CF_4 discharge: effect of gas composition *J. Appl. Phys.* **93** 2369

[38] Nanbu K 2000 Probability theory of electron–molecule, ion–molecule, molecule–molecule and Coulomb collisions for particle modeling of materials processing plasmas and gases *IEEE Trans. Plasma Sci.* **28** 971

[39] Lieberman M A and Lichtenberg A J 1994 *Principles of Plasma Discharges and Materials Processing* (New York: Wiley)

[40] Vincenti W G and Kruger C H Jr 1965 *Introduction to Physical Gas Dynamics* (New York: Wiley)

[41] Matsunami N, Yamamura Y, Itikawa Y, Itoh N, Kazumata Y, Miyagawa S, Morita K, Shimizu R and Tawara H 1984 Energy dependence of the ion-induced sputtering yields of monatomic solids *At. Data Nucl. Data tables* **31** 1

[42] Mahieu S, Van Aeken K, Depla D, Smeets D and Vantomme A 2008 Dependence of the sticking coefficient of sputtered atoms on the target–substrate distance *J. Phys. D: Appl. Phys.* **41** 152005

[43] Kubart T, Kappertz O, Nyberg T and Berg S 2006 Dynamic behaviour of the reactive sputtering process *Thin Solid Films* **515** 421

[44] Greenwood J 2002 The correct and incorrect generation of a cosine distribution of scattered particles for Monte-Carlo modelling of vacuum systems *Vacuum* **67** 217

[45] Kolev I 2007 Particle-in-cell–Monte Carlo collisions simulations for a direct current planar magnetron discharge *PhD Thesis* University of Antwerp

[46] Depla D, Li X Y, Mahieu S and De Gryse R 2008 Determination of the effective electron emission yields of compound materials *J. Phys. D: Appl. Phys.* **41** 202003

[47] Depla D, Mahieu S and De Gryse R 2009 Magnetron sputter deposition: linking discharge voltage with target properties *Thin Solid Films* **517** 2825

[48] Kolev I and Bogaerts A 2008 Calculation of gas heating in a dc sputter magnetron *J. Appl. Phys.* **104** 093301

[49] Hirschfelder J O, Curtiss C F and Bird R B 1964 *Molecular Theory of Gases and Liquids* (New York: Wiley)

[50] Zhen S and Davies G J 1983 Calculation of the Lennard–Jones n–m potential energy parameters for metals *Phys. Status Solidi.* a **78** 595

[51] Svehla R A 1962 Estimated viscosities and thermal conductivities of gases at high temperatures *National Aeronautics and Space Administraion (NASA), Technical Report* p R–132

[52] Mahieu S 2009 Measurements at Ghent University, Private communications

[53] ftp://jila.colorado.edu/collision_data/electronneutral/hayashi.txt

[54] Phelps A V and Petrovic Z Lj 1999 Cold-cathode discharges and breakdown in argon: surface and gas phase production of secondary electrons *Plasma Sources Sci. Technol.* **8** R21

[55] Mason N J and Newell W R 1987 Total cross sections for metastable excitation in rare gases *J. Phys. B: At. Mol. Opt. Phys.* **20** 1357

[56] Eggarter E 1975 Comprehensive optical and collision data for radiation action. II. Ar* *J. Chem. Phys.* **62** 833

[57] Hyman H A 1979 Electron-impact ionization cross sections for excited states of the rare gases (Ne, Ar, Kr, Xe), cadmium and mercury *Phys. Rev.* A **20** 855

[58] Hyman H A 1978 Electron-impact excitation of metastable argon and krypton *Phys. Rev.* A **18** 441

[59] Vriens L 1964 Calculation of the absolute ionisation cross sections of He, He*, He$^+$, Ne, Ne*, Ne$^+$, Ar, Ar*, Hg and Hg* *Phys. Lett.* **8** 260

[60] ftp://jila.colorado.edu/collision_data

[61] De Bleecker K, Herrebout D, Bogaerts A, Gijbels R and Descamps P 2003 One-dimensional modelling of a capacitively coupled rf plasma in silane/helium, including small concentrations of O_2 and N_2 *J. Phys. D: Appl. Phys.* **36** 1826

[62] Guerra V and Loureiro J 1999 Kinetic model of a low-pressure microwave discharge in O_2–N_2 including the effects of O-ions on the characteristics for plasma maintenance *Plasma Sources Sci. Technol.* **8** 110

[63] Kossyi A, Kostinsky A Y, Matveyev A A and Silakov V P 1992 Kinetic scheme of the non-equilibrium discharge in nitrogen–oxygen mixtures *Plasma Sources Sci. Technol.* **1** 207

[64] Tinck S, Boullart W and Bogaerts A 2009 Investigation of etching and deposition processes of $Cl_2/O_2/Ar$ inductively coupled plasmas on silicon by means of plasma–surface simulations and experiments *J. Phys. D: Appl. Phys.* **42** 095204

[65] Phelps A V 1994 The application of scattering cross sections to ion flux models in discharge sheaths *J. Appl. Phys.* **76** 747

[66] Phelps A V 1991 Cross sections and swarm coefficients for nitrogen ions and neutrals in N_2 and argon ions and neutrals in Ar for energies from 0.1 eV to 10 keV *J. Phys. Chem. Ref. Data* **20** 557

[67] Bogaerts A and Gijbels R 1996 Role of sputtered Cu atoms and ions in a direct current glow discharge: combined fluid and Monte Carlo model *J. Appl. Phys.* **79** 1279

[68] Rauf S and Kushner M J 1997 Argon metastable densities in radio frequency Ar, Ar/O$_2$ and Ar/CF$_4$ electrical discharges *J. Appl. Phys.* **82** 2805

[69] Ferreira C M and Ricard A 1983 Modelling of the low-pressure argon positive column *J. Appl. Phys.* **54** 2261

[70] Ferreira C M, Loureiro J and Ricard A 1985 Populations in the metastable and the resonance levels of argon and stepwize ionization effects in a low-pressure argon positive column *J. Appl. Phys.* **57** 82

[71] Riseberg L A, Parks W F and Schearer L D 1973 Penning ionization of Zn and Cd by noble-gas metastable atoms *Phys. Rev.* A **8** 1962

[72] Tachibana K 1986 Excitation of the 1s$_5$, 1s$_4$, 1s$_3$, 1s$_2$ levels of argon by low-energy electrons *Phys. Rev.* A **34** 1007

[73] Phelps A V, Greene C H and Burke J P Jr 2000 Collision cross sections for argon atoms with argon atoms for energies from 0.01 eV to 10 keV *J. Phys. B: At. Mol. Opt. Phys.* **33** 2965

[74] Phelps A V and Jelenkovic B M 1988 Excitation and breakdown of Ar at very high ratios of electric field to gas density *Phys. Rev.* A **38** 2975

[75] Robinson R S 1979 Energetic binary collisions in rare gas plasmas *J. Vac. Sci. Technol.* **16** 185